Journal of Materials Chemistry A

ROYAL SOCIETY OF CHEMISTRY

PAPER

View Article Online
View Journal | View Issue

Open Access Article. Published on 09 February 2026. Downloaded on 5/6/2026 9:41:51 PM.
This article is licensed under a Creative Commons Attribution 3.0 Unported Licence.

Check for updates

Cite this: J. Mater. Chem. A, 2026, 14, 11344

# Nanoengineering 2D ceria-perovskite monolayers on $SrTiO_3$ nanocubes: structure-redox property relationship

Ramón Manzorro,[ab] Jose M. Montes-Monroy,[ab] Carmen Mora-Moreno,[ab] Lidia E. Chinchilla,[ab] Ana B. Hungría,[ab] Jose J. Calvino[ab] and Jose A. Pérez-Omil *[ab]

Achieving the full potential of ceria-based catalysts relies on maximizing the utilization of the $Ce^{4+}/Ce^{3+}$ redox couple. This study presents a strategy to synthesize highly efficient catalysts by epitaxially dispersing cerium oxide onto strontium titanate ($SrTiO_3$) nanocubes. Leveraging the structural compatibility between the fluorite ($CeO_2$) and perovskite ($SrTiO_3$) structures, revealed by atomic resolution scanning transmission electron microscopy, reductive thermal treatments are used to generate two-dimensional (2D) ceria-perovskite nano-overlayers—precisely one unit-cell thick—that uniformly cover the $SrTiO_3$ support. This atomic-scale control results in a catalyst system that achieves 100% cerium redox utilization, exhibiting significantly enhanced reducibility and a stabilized surface compared to bulk ceria. The experimental evidences are corroborated by density functional theory calculations. This work establishes a robust foundation for designing lanthanide-lean catalysts with superior chemical properties by exploring analogous fluorite-perovskite support interfaces.

Received 23rd October 2025
Accepted 6th February 2026

DOI: 10.1039/d5ta08625f

rsc.li/materials-a

## 1 Introduction

Cerium oxide is widely used for its catalytic applications. Cerium's ability to switch between the +3 and +4 oxidation states, and therefore the possibility of creating oxygen vacancies, is key to understanding its remarkable performance in applications involving oxygen capture/release.[1–3] The oxygen storage capacity together with the reducibility may be extended and improved when cerium is mixed with zirconium, specially when the formation of pyrochlore-type phases takes place.[4–6]

More recently, the design of catalytic systems has aimed at optimizing the nanostructure of active surface phases, which allows both decreasing the lanthanide loading and maximizing its dispersion. In the particular case of cerium catalysts, a load equivalent to a quarter of a cerium oxide monolayer on a cubic yttrium-stabilized zirconia (YSZ), that preferentially exposes (111) planes, has been recently reported.[7] After applying a severe reduction treatment, followed by a mild oxidation, the so-called SRMO treatment,[8] an oxidised zirconium-rich pyrochlore monolayer supported in perfect epitaxial relationship onto the YSZ support is generated, where the Ce cations are assembled as single atoms. This particular arrangement provides full exposure of the lanthanide phase at the surface (100% utilization), while preserving the typical improvements in low-temperature reducibility of the aforementioned oxidised pyrochlore phases. DFT calculations have demonstrated that the mechanism responsible for the enhanced reducibility of this system is also valid for Ce/Zr pyrochlore 3D nanocrystals obtained following an SRMO treatment. These nanocrystals exhibit an alternation of Zr-rich and Ce-rich (111) planes in the bulk, with a Zr-rich (111) surface being exposed.[7]

The pyrochlore (111) monolayer is formed through epitaxial growth on the (111) planes of the YSZ support, displaying $C_6$ symmetry. This observation indicates a significant influence of the underlying support's surface structure on the emergent cerium-based nanostructure. Consequently, a pertinent question arises: would the utilization of an alternative support with a distinct surface structure differentially impact the nanostructure of ceria-based monolayers and their inherent chemical, specifically redox, properties?

Strontium titanate is a compound that is considered the archetypal perovskite structure. It crystallizes at room temperature in the cubic system, according to the *Pm*-3*m* space group.[9] It is a very frequently used material due to its photocatalytic and optical properties, its low cost and lack-of toxicity, its high thermal stability and resistance to corrosion and also due to its particular dielectric properties.[10–14] All these properties can be modulated by controlling both bulk/surface defects[15–17] and the morphology of the $SrTiO_3$ nanoparticles.[18,19] Particularly, it has already been reported that the deposition of surface phases

[a]Departamento de Ciencia de los Materiales e Ingeniería Metalúrgica y Química Inorgánica, Facultad de Ciencias, Universidad de Cádiz, 11510-Puerto Real, Spain. E-mail: jose.perez-omil@uca.es

[b]Instituto de Microscopía Electrónica y Materiales (IMEYMAT), Facultad de Ciencias, Universidad de Cádiz, 11510-Puerto Real, Spain

 This journal is © The Royal Society of Chemistry 2026

Open Access Article. Published on 09 February 2026. Downloaded on 5/6/2026 9:41:51 PM.
This article is licensed under a Creative Commons Attribution 3.0 Unported Licence.

modifies the properties of $SrTiO_3$.[20] In this scenario, it stems as a good candidate to be used as a substrate of monolayer-type surface phases.

Epitaxial growth is a key factor in the current development of surface phases. This type of growth is strongly influenced by the structural coherence at the interface between the support and surface phases. For nanopowder substrates, controlling this can be quite challenging due to the wide variety of crystallographic terminations these materials typically exhibit. However, using morphology-controlled support nanoparticles may help overcome this limitation. In this regard, it is important to note that $SrTiO_3$ has been previously synthesized as {100}-bounded nanocubes using hydrothermal methods.[21–24] Moreover, given the polar nature of this particular crystallographic plane in this structure, the surface of the nanocubes can be tuned to expose either Sr or Ti.[25]

A simple analysis suggests that the atomic structure of $SrTiO_3$ (001) planes may lead to an epitaxial relationship with the (001) plane of $CeO_2$ as has been already reported,[26–28] due to the same ($C_4$) symmetry and quite similar distances between oxygens in these two planes, 3.91 Å and 3.82 Å, respectively, when a 45° rotation is applied between the two phases.

All in all, (001)-bounded $SrTiO_3$ nanocubes appear to be an ideal support to explore the dispersion of cerium oxide on their surface and study the effect of redox treatments on the reducibility and other properties of the resulting supported ceria phase.[29,30] With these questions in mind, this work explores the possibility of supporting cerium oxide monolayers onto (001)-type strontium titanate surfaces with $C_4$ symmetry. It also aims to characterize the nanostructures formed at the atomic level, before and after SRMO treatments, and the effect that these nanostructures may have on the reducibility of the lanthanide phase.

The final outcomes related to the ceria features and behaviour observed on the $SrTiO_3$ surface will be compared to those reported on ceria over the YSZ substrate, where the planes involved are (111)-type with surface atomic arrangement giving rise to a $C_6$ symmetry. In addition, and in line with the $CeO_2$/YSZ results, it is worth asking if the application of SRMO type treatments in the $CeO_2/SrTiO_3$ system will also generate mixed phases, with improving reducibility, between the lanthanide phase and the perovskite, analogous to the pyrochlore structure characterized in the $CeO_2$/YSZ system.[7,8,31]

# 2 Experimental

## 2.1 Synthesis of the samples

$SrTiO_3$ nanocubes were prepared through microwave-assisted method, adapting the procedure described elsewhere.[32] Initially, 2.43 g of $Sr(OH)_2 \cdot 8H_2O$ (99%, Alfa Aesar) is added to a 35 mL of a solution of acetic acid in Milli-Q water with a volumetric ratio 1 : 0.06. The solution was placed in a 250 mL beaker, where 1 mL of $TiCl_4$ (99%, Fisher Scientific) previously dissolved in 15 mL of absolute ethanol was subsequently added. This mixture was stirred for 30 minutes at 300 rpm, obtaining an homogeneous transparent solution. Then, 5 g of NaOH (98%, Scharlab) were dropped also under stirring for 30 minutes. The resulting hydroxide gel (with an opaque texture) was transferred to a hydrothermal Teflon reactor. The reactor was microwaved-heated up to 220 °C at 10 °C $min^{-1}$, keeping the targeted temperature for 30 minutes with continuous stirring (100 rpm) during the whole process. Afterwards, the reactor freely cooled down to room temperature in air and the products were filtered and washed with Milli-Q water and ethanol. The final white precipitate was dried in an oven at 90 °C for 18 hours and calcined in a muffle furnace at 300 °C for 1 hour to eliminate potential contamination from the synthesis process. The chosen temperature is lower enough to prevent changes in the morphology. However, water or carbonates retained in the structure were not totally removed as will be shown in this work.

Synthesized $SrTiO_3$ nanocubes have a specific surface area calculated by the BET method of 25.0 $m^2\ g^{-1}$. The measured Sr/Ti ratio (52/48) obtained by X-ray fluorescence (XRF) analysis confirms the 1 : 1 ratio of Sr and Ti expected for this material.

For a typical preparation of a $CeO_2/SrTiO_3$ sample[1,2] (ceria loading equivalent to half a theoretical monolayer) a mass of 0.0615 g of cerium(III) nitrate hexahydrate was weighed and dissolved in 40 mL of Milli-Q water in a beaker under stirring for 20 minutes. Subsequently, 1 g of previously prepared $SrTiO_3$ nanoparticles was added, and the suspension was stirred for an additional 20 minutes. The pH was adjusted to 10 by dropwise addition of a 30% ammonia solution, monitoring the process with a pH-metre. At this stage, a color change from white to yellowish was observed, indicating the onset of cerium precipitation. The final volume was adjusted to 50 mL with water before transferring the mixture to the hydrothermal reactor. The system was microwaved-heated up to 180 °C using a rate of 10 °C $min^{-1}$ and maintained at this temperature for one hour. Finally, the resulting solid was filtered, dried in an oven, ground into a fine powder, and calcined for 1 hour at 400 °C.

Experimental X-ray Fluorescence (XRF) measurements indicate a ceria loading of 1.9 wt%. Considering the BET surface of $SrTiO_3$ and the average planar density of the cerium dioxide surface (7.5 Ce atoms per $nm^2$), a theoretical coverage of 0.41 monolayers on the support was achieved, which was lower than the targeted half-monolayer.

Finally, both the $SrTiO_3$ and $CeO_2/SrTiO_3$ samples underwent a severe reduction (SR) followed by a mild oxidation (MO), resulting in the $SrTiO_3$-SRMO and $CeO_2/SrTiO_3$-SRMO samples. This redox treatment, referred to as SRMO, basically consists of a severe reduction at 900 °C under a $H_2$(5%)/Ar atmosphere for one hour, followed by a one-hour mild oxidation at 500 °C under an $O_2$(5%)/He flow.[33]

## 2.2 Macroscopic characterization

To assess the composition, structure, and morphology of the prepared samples, different approaches were followed. The crystal structure of the synthesized powders was investigated by means of X-ray diffraction (XRD), using a D8 Advance A25 diffractometer and measuring every 0.05°. The analysis of the diffraction patterns was carried out with the freely available PowderCell software.[34] On the other hand, the macroscopic chemical composition was determined by X-ray fluorescence

Open Access Article. Published on 09 February 2026. Downloaded on 5/6/2026 9:41:51 PM. This article is licensed under a Creative Commons Attribution 3.0 Unported Licence.

(XRF) spectroscopy using a Bruker M4 Tornado Micro-XRF spectrometer. To further investigate the chemical state of the elements present in the sample, X-ray photoelectron spectroscopy (XPS) were performed, registering the spectra on a Kratos Axis Ultra DLD spectrometer and processing the data with CasaXPS software.[35] A first analysis of the $SrTiO_3$ morphology has been extracted from scanning electron microscopy (SEM), acquiring secondary electron microscopy images on a Nova NanoSEM 450 microscope, which was operated at 5 kV.

The reducibility of as prepared $SrTiO_3$, $SrTiO_3$-SRMO, $CeO_2$/$SrTiO_3$ and $CeO_2$/$SrTiO_3$-SRMO samples was evaluated under $H_2$ flow by monitoring both $H_2$ consumption and $H_2O$ formation during temperature-programmed reduction (TPR) experiments. To this end, a total amount of 150–200 mg of sample was deposited in a U-shaped quartz reactor. To measure the reducibility, a $H_2$(5%)/Ar gas mixture was flowed continuously through the reactor while increasing the temperature up to 900 °C and maintaining it there for 1 hour. The $H_2O$ formation was registered in a mass spectrometer (MS) using a Thermostar GSD301T1 (Pfeiffer), and the $H_2$ consumption was measured with a thermal conductivity detector (TCD) available in the AutoChem II (Micromeritics Instrument Corporation). Prior to the experiments, a cleaning step was applied by exposing the loaded reactor to an $O_2$/He flow up to 300 °C and holding it at that temperature for 1 hour. All gas flows were set to 60 mL $min^{-1}$ and every temperature ramp to 10 °C $min^{-1}$.

### 2.3 Scanning/transmission electron microscopy characterization

To characterize the samples *via* transmission electron microscopy, the powder was loaded into carbon-coated copper grids. The scanning/transmission electron microscopy (STEM) studies were performed in a double aberration-corrected Thermo Fisher Titan Cubed Themis 60–300 and Thermo Fisher Talos FX200 G2 microscopes, both operated at 200 kV. Sub-angstrom resolution high angle annular dark field (HAADF) images were registered after properly correcting the aberrations (spherical aberration $C_s$, 0.001 mm; fifth-order spherical aberration, 5 mm; convergence semi-angle, 19 mrad). The images were acquired with 2.5 μs per pixel and a size of 2048 × 2048 pixels, with beam currents of the order of 30 pA.

From an analytical point of view, energy dispersive X-ray spectroscopy (XEDS) elemental mapping was carried out registering the Ti–K, Sr–K and Ce–L signals using the Super X-G2 detector, using a beam current in the 120–140 pA range and a dwell time per pixel of roughly 100 μs. To further improve the visualization of the elemental maps, gaussian or radial Wiener filters were used as available in the Velox software. In the case of electron energy loss spectroscopy (EELS), the Ce-$M_{4,5}$ (883 eV) and Ti-$L_{2,3}$ (456 eV) edges were acquired working in the so-called spectrum-imaging (SI) mode. The EELS spectra were recorded with an energy dispersion of 0.25 eV/channel (reaching an energy resolution of 0.9–1 eV), 50–70 mrad of collection semi-angle, probe currents below 30 pA and 100 ms acquisition time per EELS spectrum.

The identical location STEM (IL-STEM) experiments were accomplished by depositing the sample on a 9-window $Si_3N_4$ grid with a thickness of 50 nm, placing the grid in a conventional chemical reactor and studying the same region in the microscope before and after the SRMO thermal treatment.

A DENS solutions equipment was used to characterize the $CeO_2$/$SrTiO_3$ sample *in situ*. For this purpose, 1 mg of the powder was dispersed in 5 mL of isopropanol, and a drop of the resulting solution was deposited onto the microheater. The final nanoreactor was assembled, and the sample was subjected to 900 °C in a 50% $H_2$ flow (balanced with $N_2$) and pressures close to 1 bar. To avoid contamination on the chip membrane, a previous cleaning step of 1 hour was carried out at 250 °C in 50% $O_2$ and 50% $N_2$. The structural evolution of the sample was tracked in TEM mode.

### 2.4 Modelling and density functional theory calculations

The interpretation of atomic resolution images was assisted by Eje-Z software,[36] while the design and construction of atomic models was handled with the Rhodius software,[37] which allows a total control of the orientation, the morphology, and the atomic positions of the nanostructures. Both softwares are freely available online at the TEMserver web.[38] From these atomic models, STEM images were simulated using the Computem software.[39] The specific electron-optical parameters input in the simulations are described where appropriated.

The DFT calculations included in this work have been performed using the plane-wave code Quantum Espresso with the spin polarized Perdew–Burke–Ernzerhof functional (PBE).[40] Appropriate PAW scalar relativistic pseudopotentials were used for the elements present in the models.[41] In the case of Ce, the PAW pseudopotential available in the Rare Earth database from Columbia University is chosen for DFT + U calculations.[42] The Hubbard U parameter for the Ce-4f states was determined using the density-functional perturbation theory (DFPT) implementation within the HP code. A value of 3.5 eV was ultimately selected, following the methodology described elsewhere.[7,43] The convergent wave function cut-off was calculated to be 70 Rydberg. For *K*-point integrations a 8 × 8 × 8 Monkhorst–Pack grid was used for calculations of the unit cells of bulk systems, while 2 × 2 × 1 grid or just gamma point was used for the calculations using supercells, depending on size. For the relaxation processes the Broyden–Fletcher–Goldfarb–Shanno (BFGS) algorithm for geometry optimization included in Quantum Espresso code was used, keeping unrelaxed the botton planes in the supercell models.

## 3 Results and discussions

### 3.1 Macroscopic characterization of the samples

Firstly, to characterize the macroscopic crystallographic structure of the phases present in the studied samples (fresh and after being subjected to a severe reduction mild oxidation treatment, SRMO), X-ray diffraction (XRD) patterns were recorded for all of them: $SrTiO_3$, $SrTiO_3$-SRMO, $CeO_2$/$SrTiO_3$ and $CeO_2$/$SrTiO_3$-SRMO samples (Fig. S1). As expected, the XRD

Open Access Article. Published on 09 February 2026. Downloaded on 5/6/2026 9:41:51 PM.
This article is licensed under a Creative Commons Attribution 3.0 Unported Licence.

pattern confirms the formation of the cubic $SrTiO_3$ perovskite. A negligible peak at 25.22° in the fresh $SrTiO_3$ and $CeO_2/SrTiO_3$ samples suggests the presence of strontium carbonates, although they represent less than 5 wt%. The refined lattice parameter and crystallite size of the strontium titanate are 3.91 Å and 49.3 nm, respectively. This crystallite size is consistent with the 47 ± 6 nm measured from SEM/TEM images (Fig. S2).

The analysis of TEM images (Fig. 1a) reveals that the nanocubes are not perfectly formed; they possess large inner pores and a chamfered cube morphology. Consequently, in addition to the {001} planes on the faces, {110} planes are present at the edges and, to a lesser extent, {111} planes at the corners of the cube. Based on a rough estimation of the bevels' size, we calculated approximately 30% {110} and 4% {111}-type surface terminations, as shown in Fig. S3.

Conversely, Fig. 1b shows that nanocubes in the $SrTiO_3$-SRMO sample have undergone noticeable sintering, growing from 47 nm to 95 nm and largely losing their initial morphology. This phenomenon, likely promoted by the self-diffusion of surface atoms from edges or corners to the (001) facets, aims to minimize the surface free energy of the nanoparticle ensemble.

In contrast, Fig. 1c and e demonstrate that the $CeO_2/SrTiO_3$ and $CeO_2/SrTiO_3$-SRMO samples maintain similar average sizes, 52 nm and 56 nm, respectively. This indicates that adding ceria promotes textural stability, even under reducing conditions at temperatures as high as 900 °C, which aligns well with reported data for a $CeO_2$/Au/YSZ sample.[44] XEDS elemental maps (Fig. 1d and f) indicate that ceria nanoparticles have redispersed after the SRMO thermal treatment, a topic we will discuss further below.

In addition, the Ti 2p XPS spectra of these samples (Fig. S4a) exclusively exhibit $Ti^{4+}$, indicating that titanium is not reduced following SRMO treatment, consistent with the findings of Shetty *et al.*[32] Regarding cerium (Fig. S4b), the Ce 3d spectra correspond to a predominantly reduced phase in both ceria-containing samples. However, the potential reduction of this element due to sample handling or X-ray-induced reduction cannot be entirely ruled out. It should be noted that the ceria loading remains below the theoretical monolayer capacity and is dispersed across the entire surface. This low loading, coupled with the small particle size, precludes a reliable quantitative XPS analysis of the evolution of phase dispersion and oxidation states following SRMO treatment.

The redox properties of these catalysts were evaluated *via* temperature-programmed reduction experiments with hydrogen, following $H_2O$ release with a mass spectrometer (MS) and $H_2$ consumption with a TCD detector, as shown in Fig. 2a and b, respectively.

First, water loss from the $SrTiO_3$ support begins at a very low temperature (250 °C), with peaks at 350 °C, 550 °C, and 750 °C, the latter being the most intense event. However, its $H_2$ consumption profile only exhibits a peak at high temperature, similar to the one observed at the third peak in the water profile. Therefore, these two experiments suggest that the broad, low-temperature water release peaks at 350 °C and 550 °C correspond to either hydration water or the condensation of hydroxyl groups, rather than the reduction of the support *via* the creation

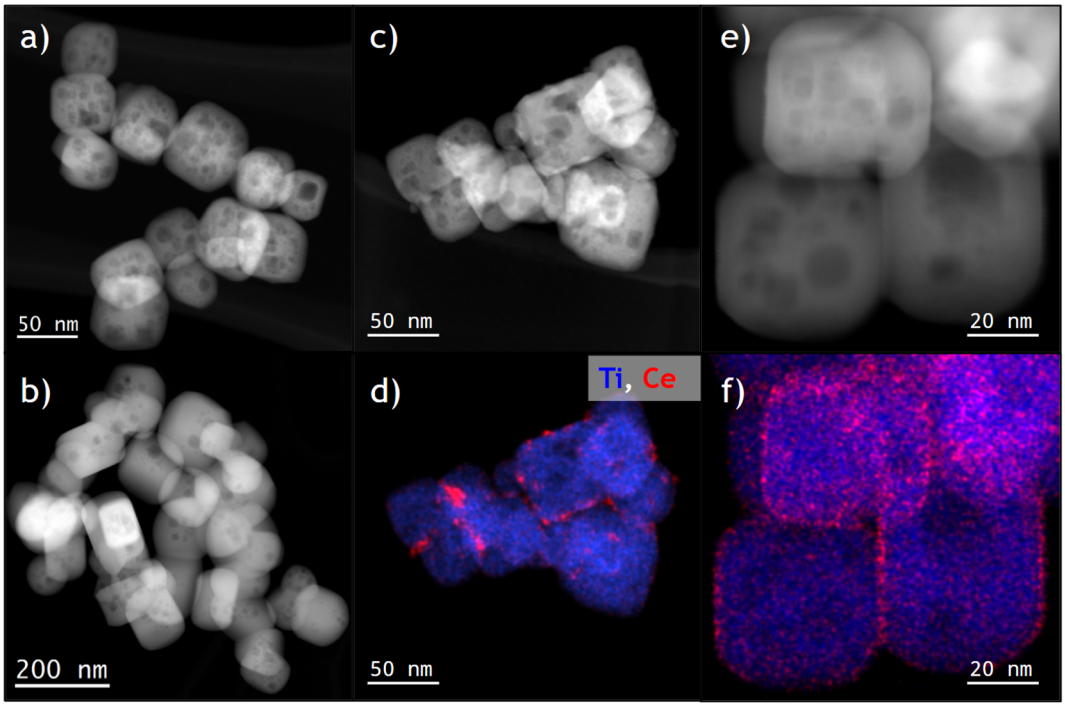


Fig. 1 STEM characterization at medium-low magnification. (a) and (b) HAADF images corresponding to the $SrTiO_3$ support and $SrTiO_3$-SRMO, respectively. (c–f) HAADF images along with their corresponding XEDS elemental maps for the $CeO_2/SrTiO_3$ sample and $CeO_2/SrTiO_3$-SRMO, respectively. The Ti and Ce elements in the XEDS maps are represented in blue and red, in that order.

Open Access Article. Published on 09 February 2026. Downloaded on 5/6/2026 9:41:51 PM.
This article is licensed under a Creative Commons Attribution 3.0 Unported Licence.

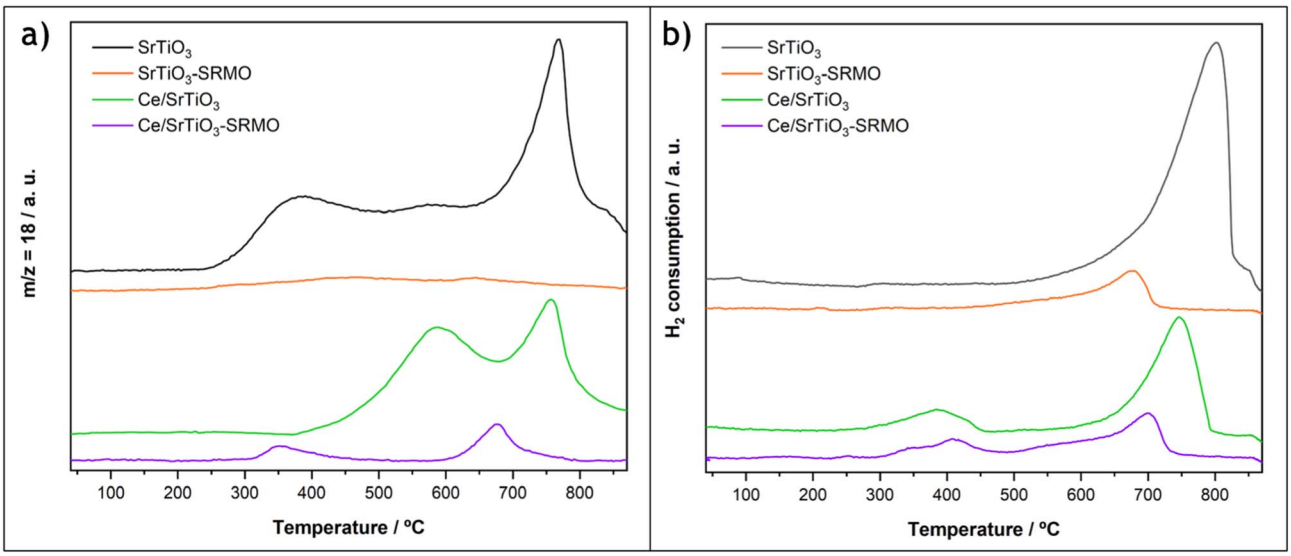


Fig. 2 Reduction of the $SrTiO_3$, $SrTiO_3$-SRMO, $CeO_2/SrTiO_3$ and $CeO_2/SrTiO_3$-SRMO samples under $H_2$(5%)/Ar atmosphere. (a) Qualitative TPR profile registering water release (mass to charge ratio $m/c = 18$ signal), recorded with a mass spectrometer. (b) Quantitative TPR profile measuring hydrogen consumption and recorded with a TCD detector.

of oxygen vacancies. This finding is consistent with the low calcination temperature used to prepare the $SrTiO_3$ substrate. For the high-temperature peak, $H_2$ uptake and water release are concomitant with CO release (Fig. S5), indicating that this event corresponds to carbonate reduction, which aligns well with the detection by XRD of a small porcentage of carbonates in the fresh sample.

In contrast, the $SrTiO_3$-SRMO sample shows a practically flat and horizontal line in the water signal. Since the SRMO treatment and the MS-TPR experiment were run consecutively and the sample was not exposed to air during the entire process, there is a lack of adsorbed water and carbonates in the registered data for this sample (Fig. 2a). However, this is not the case for the TCD-TPR experiment (Fig. 2b), where the $SrTiO_3$-SRMO sample was exposed to air after the thermal treatment, and a small peak detected at approximately 700 °C is probably due again to surface carbonates.

For the ceria-modified samples, the water profile of $CeO_2/SrTiO_3$ shows two maxima: one peaking at 550 °C and another centered at 750 °C. It should be noted that the sample was subjected to an oxidation treatment at 400 °C after $CeO_2$ deposition. As a result, a portion of the hydration water and hydroxyl groups measured in the bare $SrTiO_3$ sample were already eliminated. However, a significant fraction is still released above that temperature. The first broad peak in the $CeO_2/SrTiO_3$ water profile at 550 °C represents the combined contribution of the oxygen vacancy formation in the ceria phase, which typically occurs at around 450 °C in highly-dispersed systems, in good agreement with the $H_2$ consumption at lower temperature, and the remaining hydration water and hydroxyl groups. Finally, the water release at higher temperatures (750 °C) occurs in parallel with another $H_2$ uptake and the emission of CO, which is attributed to the decomposition of carbonates, similar to the bare $SrTiO_3$ sample. The amount of $H_2$ consumed in this second peak for the $CeO_2/SrTiO_3$ sample is roughly three times smaller than that of the ceria-free sample, suggesting that the deposition of the lanthanide phase partially eliminates the $SrTiO_3$ carbonation.

On the other hand, the $CeO_2/SrTiO_3$-SRMO sample also exhibits two reduction events, with peaks at 350 °C and 700 °C. The high-temperature maximum at 700 °C corresponds to the reduction of carbonates, as the sample was exposed to air this time before both the mass spectrometry (MS) and thermal conductivity detector (TCD) $H_2$-TPR experiments.

More interestingly, and in contrast to the $CeO_2/SrTiO_3$ sample, the 350 °C peak shows a simultaneous release of water and uptake of $H_2$, indicating that $H_2$ activation and the formation of oxygen vacancies occur concurrently. The quantitative analysis of this low-temperature $H_2$ consumption peak is nearly equivalent to the reduction of all the deposited $Ce^{4+}$. Furthermore, the onset of the reduction peak associated with water release and $O_2$ vacancy formation is shifted by 100 °C to a lower temperature compared to the typical highly dispersed ceria phase. This observation suggests that the supported lanthanide phase undergoes a modification after the SRMO treatment, making it more reducible under $H_2$ flow.

### 3.2 Atomic resolution STEM study and DFT calculations of the samples before SRMO treatment

The crystal structure of the perovskite along the [001] zone axis was clearly identified at the atomic level using HAADF, XEDS, and iDPC experiments combined with image simulations (Fig. S6). The characterization of the nanocube surfaces confirms the presence of {001} crystallographic terminations, which in all cases expose a SrO plane in the outermost layer (Fig. 3a). A visual inspection of the intensities of this outermost plane suggests a lighter contrast compared to the bulk, with column intensities that are not uniformly distributed. This drop

Open Access Article. Published on 09 February 2026. Downloaded on 5/6/2026 9:41:51 PM.
This article is licensed under a Creative Commons Attribution 3.0 Unported Licence.

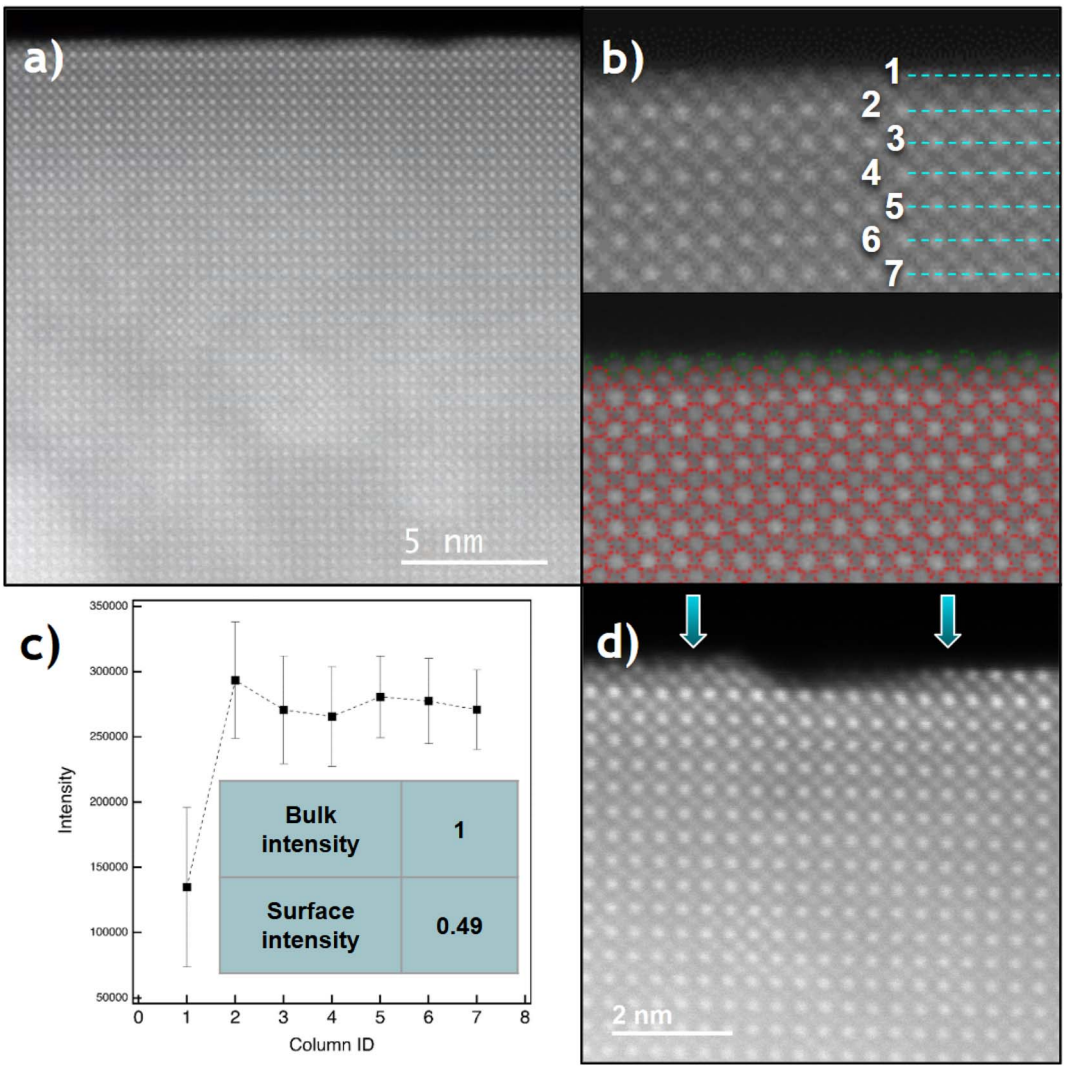


Fig. 3 Analysis of the {100} surface of the $SrTiO_3$ cubes. (a) High resolution HAADF image showing a noticeable decrease in contrast at the topmost surface. (b) Zoomed HAADF image where the cations columns have been tracked to measure their intensities and roughly estimate the Sr column occupation. (c) Graph representing the average intensity of the columns at different atomic planes, from the surface to the interior of the cube (1 to 7, in that order). (d) HAADF image indicating the existence of Ti–Sr double steps, which always end in Sr.

in intensity from atomic columns at the surface has been previously observed by Du and collaborators.[45] Fig. 3b and c show that the average measured intensity of Sr columns in this surface layer drops by approximately 50% compared to the bulk Sr sites. This dip suggests a large number of Sr-vacancies (close to 50%) and the corresponding O-vacancies in the last Sr layer. This result is reasonable, given that the chemical ratio of the Ti and Sr elements is 1 : 1 and all {001} type surfaces terminate in Sr. Fig. 3d shows the occasional presence of double Ti–Sr steps, with Sr always at the outermost surface (see blue arrows). Furthermore, the intensity profile perpendicular to the surface from Fig. S7 indicates that the last Sr layer is slightly contracted (<2%). The (001) surface relaxation calculated in this work *via* DFT confirms that the final (001) *d*-spacing contracts by 4.1% (from 3.91 to 3.75 Å) for a fully occupied Sr layer.

In the $CeO_2/SrTiO_3$ sample, the lanthanide phase is arranged in the form of nm-sized nanoparticles, with an average diameter of 5.0 ± 1.1 nm, as previously shown in Fig. 1c and d. High resolution STEM images reveal a perfect epitaxy relationship at the interface between the (001) terminations of both ceria and $SrTiO_3$, observing a parallel growth of the $CeO_2$ nanoparticles' (001) planes on the (001) surfaces of the support (Fig. 4a–d). However, [110] and [100]-like zone axes are observed for $CeO_2$ and $SrTiO_3$, respectively, which reveals a 45° rotation between the two structures. This finding is in good agreement with the $C_4$-like arrangement of Sr or Ce found for the (001) planes in both structures.[26–28] The structural relationship between the two phases, $(001)_{CeO_2}//(001)_{SrTiO_3}$ and $[110]_{CeO_2}//[100]_{SrTiO_3}$, hereafter referred to as AA45 epitaxy, is quite smooth. Only a 2% expansion in the ceria *XY* plane is needed to achieve a perfect match (Fig. S8a). This lattice expansion could positively impact the reducibility of the ceria phase.[46]

Along the [001] zone axis, the fluorite presents alternating (001) layers of Ce and $O_2$, while the perovskite has (001) layers of

Open Access Article. Published on 09 February 2026. Downloaded on 5/6/2026 9:41:51 PM.
This article is licensed under a Creative Commons Attribution 3.0 Unported Licence.

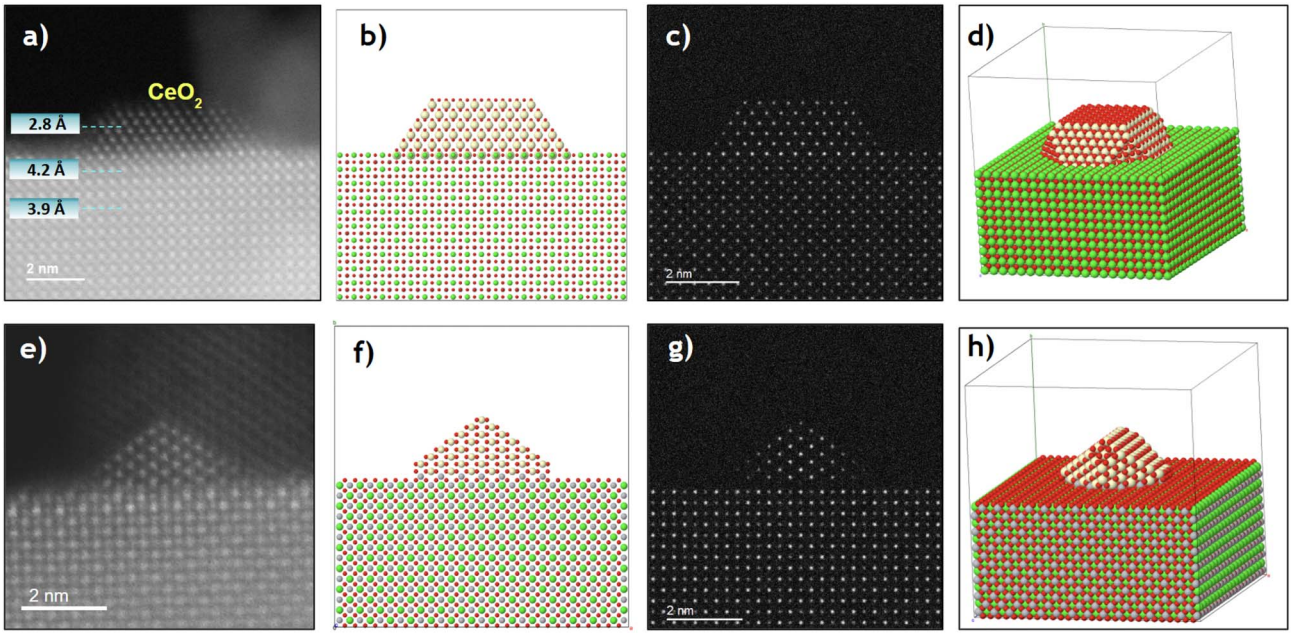


Fig. 4 Epitaxial relationships between $CeO_2$ and $SrTiO_3$. (a) Experimental HAADF image showing the epitaxial growth of a $CeO_2$ nanoparticle on top of the $SrTiO_3$ (001) surface. (b) Atomic model corresponding to the visualized situation, where the Ce, Ti, Sr and O atoms are represented in beige, green, gray and red. (c) HAADF image simulated using the μSTEM software from the present model. This simulation was subsequently treated by adding electronic noise to soften the contrasts and more closely resemble the experimental image. The following experimental conditions have been used: voltage: 200 kV, Cs3: 0.001 mm, Cs5: 5 mm, defocus: 1 nm, convergence angle: 19 mrad, HAADF angles: 80–200 mrad (d) perspective view of the model, which allows for a clearer appreciation of the $CeO_2$ particle's cuboctahedral morphology. (e–h) The corresponding images for the epitaxial relationship between $CeO_2$ and $SrTiO_3$ (110) planes.

SrO and $TiO_2$. As mentioned previously, the final plane of the perovskite terminates in a partially covered SrO layer (with roughly 50% occupancy). It is therefore reasonable to assume that Ce cations will fill some of these Sr vacancies during deposition. This would result in the coexistence of the last perovskite plane and the first fluorite planes at the interface between the $CeO_2$ nanoparticles and $SrTiO_3$ nanocubes, see Fig. S9a and b. This interface would therefore be of the type –SrO–$TiO_2$–(SrO/Ce–$O_2$)–Ce–$O_2$–, creating continuity between the cationic sublattices of both structures: the body-centered cubic (bcc) cation sublattice of the perovskite structure is aligned with the fluorite fcc (which can be visualized as a tetragonally distorted bcc lattice) present in the $CeO_2$. Furthermore, the oxygens follow this consistency between both structures.

Fig. S9c and d shows the AA45 interface before and after structural relaxation. Interestingly, after relaxation, the two fluorite planes get closer (Ce–$O_2$ → $CeO_2$) and the $TiO_2$ layer begins to split into two different planes ($TiO_2$ → Ti–$O_2$). This indicates a clear accommodation process of the perovskite to the fluorite and *vice versa*. The distance calculated after relaxation of the structure between the penultimate Sr layer and the first Ce layer (which also contains Sr) is 4.2 Å, assuming a 100% Ce occupation. This signafies an expansion of the last plane of the perovskite (from 3.91 Å), which contrasts with the contraction observed in the bare $SrTiO_3$ (001) surface.

In addition to the AA45 epitaxy described above, HAADF images show that some ceria particles are deposited at the bevels of the $SrTiO_3$ nanocubes through a new epitaxial relationship: $(110)_{CeO_2}//(110)_{SrTiO_3}$, and $[1\text{–}10]_{CeO_2}//[001]_{SrTiO_3}$ (Fig. S8b). This relationship will be referred to as BB90 epitaxy. This situation is illustrated in Fig. 4e–h, where a $CeO_2$ particle exposes (111) faces, which are compatible with a cuboctahedral shape cut through the {110} planes. The STEM images show a perfect match between the nanoparticle and the support, confirming a 2% expansion in the ceria *XY* plane. This expansion could also positively impact on the reducibility of the ceria phase.[46] In addition to the *XY* expansion, the $CeO_2$ nanoparticle slightly shrinks the (110) *d*-spacing (along the *Z* direction), while the *d*-spacing of the last perovskite plane increases notably by 12–14%.

To understand these changes, an atomic model was constructed to represent the initial $CeO_2/SrTiO_3$ interface for the BB90 epitaxy, see Fig. S10a. The perovskite structure has alternating –SrTiO–$O_2$–SrTiO–$O_2$– layers, while the fluorite exhibits –$CeO_2$–$CeO_2$– planes. When this interfacial model is submitted to DFT relaxation, similar findings comparable to the AA45 epitaxy, regarding the atomic accommodation between both structures, is observed. At the interface, the last perovskite plane unfolds, splitting the original (110) plane into two distinct planes: $SrO_2$ and TiO (Fig. S10b). Therefore, after relaxing the model, a sequence of –SrTiO–$O_2$–TiO–$SrO_2$–$CeO_2$–$CeO_2$– is observed. The TiO layer corresponds to linear chains of TiO parallel to the interface, while the Sr merges with the $O_2$, generating a new $SrO_2$ layer isostructural to fluorite $CeO_2$. It is important to note that this plane would contain a mixture of Sr and Ce. The presence of fluorite thus increases the distortion of

Open Access Article. Published on 09 February 2026. Downloaded on 5/6/2026 9:41:51 PM.
This article is licensed under a Creative Commons Attribution 3.0 Unported Licence.

the (110) facets of $SrTiO_3$, which is an effect related to that found at the $ZrO_2$(110)/$SrTiO_3$(110) interface,[47] with important implications for its dielectric and catalytic properties.

Therefore, the epitaxial relationships and the strong interaction between the $CeO_2$ and $SrTiO_3$ phases can explain the high dispersion of the lanthanide phase found experimentally.

### 3.3 Atomic resolution STEM study and DFT calculations of the samples after a SRMO treatment

Although crystal sintering was observed in the $SrTiO_3$-SRMO sample, no structural changes occurred. Even so, the sample's surface was analyzed using EELS (Fig. S11) to evaluate any remaining surface reduction caused by the strong reduction treatment. The spectrum from the bulk exhibits typical $Ti^{4+}$ features. A comparison with the surface spectrum reveals a loss in the $L_{2,3}$ fine structure along with a slight shift toward lower energies. This redshift could be attributed to the reduction of the topmost Ti species, although the broadening of the $L_{2,3}$ edges due to surface symmetry breaking or amorphization cannot be completely ruled out.[48] Consistent with this, XPS experiments previously mentioned show no evidence of Ti reduction following the SRMO treatment. Therefore, it is difficult to draw a meaningful conclusion from the analysis of EELS data.

In contrast, the $CeO_2$/$SrTiO_3$-SRMO sample has undergone significant structural modification at the surface level. Both the HAADF image and the XEDS compositional map (Fig. 5a and b) show the complete disappearance of $CeO_2$ nanoparticles. This gives rise to the formation of a Ce-based layer that extends over the entire surface of the $SrTiO_3$ nanocube.

Fig. 5c and d reveal the atomic resolution structure of this layer, which interestingly shows that ceria extends over just a single layer. This layer is not directly exposed at the surface but is instead covered by $TiO_2$ and SrO layers. This creates a sub-nanometric 2D perovskite monolayer that is only one unit cell thick.

The quantification of the Ce-based monolayer from the XEDS compositional maps indicates that Sr and Ce coexist in the same plane at a Ce/Sr ratio close to 35/65. This composition is very similar to the initial ceria loading of 0.41 monolayers, suggesting that almost the entire cerium phase is in the form of the monolayer. After normalization, the Ti/Sr relative signal increases from the bulk (~50/50) to the surface (66/34), which points to a 50% occupancy of the Sr positions. This is in good agreement with the qualitative HAADF measurements of the bare $SrTiO_3$, which had indicated the presence of 50% Sr vacancies on the surface before ceria deposition. Taking these vacancies and the Ce/Sr ratio into account, a final composition of 52% Sr, 28% Ce, and 20% cationic vacancies is proposed for the Ce–Sr layer.

Therefore, it can be hypothesized that during the strong reduction, $Ce^{3+}$ cations migrate, filling partially the $Sr^{2+}$ vacancies. This process generates the mixed Ce/Sr monolayer with some unoccupied cationic vacancies. It is worth noting that the $Ce^{3+}$ radius (1.14 Å) is very similar to the $Sr^{2+}$ radius (1.13 Å), which facilitates this accommodation. It is thus considered that a mixed $SrTiO_3$/$Ce_{2/3}TiO_3$ perovskite is formed during the reduction step, resulting in a 2D structure with a tentative composition of $Sr_{1/2}Ce_{1/3}TiO_3$ and containing 1/6 of cationic vacancies in the Sr positions. The final concentration of cation vacancies is related to the substitution of a divalent cation by a trivalent one. This is in relatively good agreement with other reported data.[49] However, the reduction of some superficial Ti and the formation of oxygen vacancies cannot be completely ruled out.

The formation of this unique structure from an energetic point of view has been studied using DFT calculations. To do this, two models were considered: one with a (001) $SrTiO_3$ surface having half of the Sr cations, and another where $Ce^{3+}$ was also introduced into one-third of the Sr positions, while leaving one-sixth of the Sr positions as cationic vacancies (Fig. S12). This matches the stoichiometry found experimentally. The localization of the electron in the $Ce^{3+}$ species was accounted for by using the appropriate Hubbard $U$ parameter.[7] The corresponding oxygen atoms were added in both models as

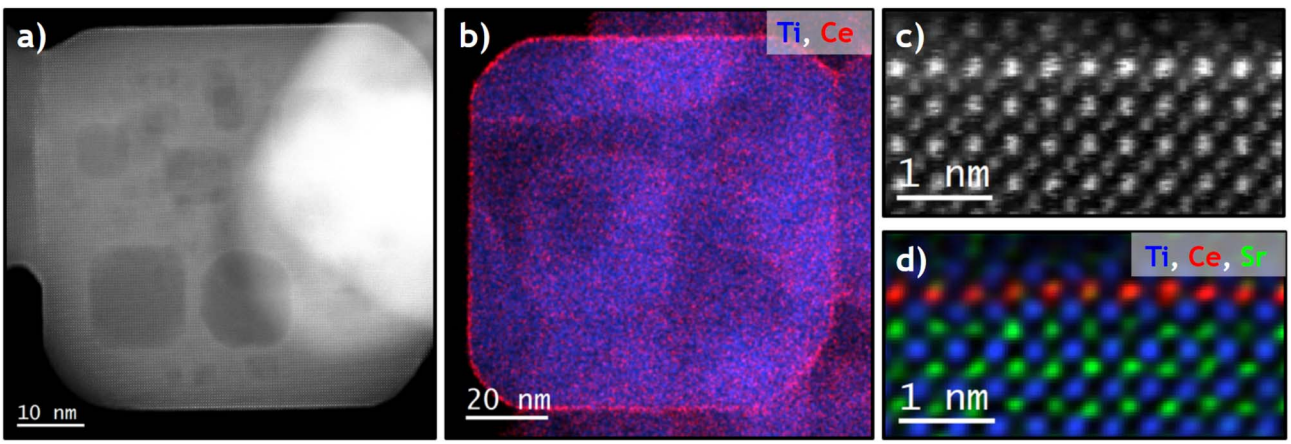


Fig. 5 High resolution STEM characterization of the $CeO_2$/$SrTiO_3$-SRMO sample. (a) and (b) Representative HAADF image and XEDS elemental map of a cube after the treatment, showing the spatial distribution of Ti (blue) and Ce (red). (c) and (d) Atomic-resolution HAADF image and XEDS map of the surface of these cubes, respectively, which demonstrates the uniformity of the Ce-rich layer.

Open Access Article. Published on 09 February 2026. Downloaded on 5/6/2026 9:41:51 PM.
This article is licensed under a Creative Commons Attribution 3.0 Unported Licence.

appropriate. After relaxation, the formation energy of the monolayer was calculated using the following equation:

$$E = 1/S\,(U_{SrCeTiO_3} - U_{SrTiO_3} - n \cdot E_{Ce_2O_3}) \quad (1)$$

where $U_{SrTiO_3}$ and $U_{SrCeTiO_3}$ correspond to the energies of the first and second models just described, after relaxation, $E_{Ce_2O_3}$ to the energy of one unit of cubic $Ce_2O_3$ (bulk), and finally $S$ is the exposed surface in the models. The final calculated energy is found to be negative, $-0.5$ J m$^{-2}$. This means that when ceria is reduced at high temperature, its dispersion across the entire surface of the support is energetically favorable, leading to the formation of the Ce–Sr monolayer.

Besides this, the lower intensity of the Ti and Sr cationic columns on top of the Ce–Sr plane, relative to the bulk, suggests that this double layer is not complete and may be due to some migration of Sr, Ti, and O ions from the {110} bevels to the {001} facets of the nanocubes after the ceria phase spreads. This migration would be caused by the natural sintering process that occurs at high temperatures.[50] Furthermore, taking into account that the nanocubes' particle size does not change after the SRMO treatment of the ceria-containing sample, we can conclude that the Sr–Ti cation migration is quite limited, to less than one double layer. Therefore, the presence of the Ce phase hinders the sintering process during the SR treatment, which preserves the morphology of the $SrTiO_3$ nanoparticles. This process only partially creates the double layer on top of the Ce-based monolayer and does not proceed further.

To probe the nature of this atomic layer, EELS experiments were performed, comparing the Ti-$L_{2,3}$ fine structure of $CeO_2$/$SrTiO_3$ and $CeO_2$/$SrTiO_3$-SRMO in both the bulk and at the surface (Fig. S11). The profiles show that $Ti^{4+}$ is detected in the bulk. However, at the surface, we observe a degraded fine structure and a nearly vanished $t_{2g}$ signal. While these surface features might suggest $Ti^{3+}$, many factors mentioned previously can alter the Ti-$L_{2,3}$ fine structure at the surface, preventing a definitive conclusion. In the case of the Ce-$M_{4,5}$ fine structure, the data suggest the presence of $Ce^{3+}$ in both samples. This is attributed to electron beam-induced reduction, facilitated by the highly dispersed nature of the ceria phase. While the presence of residual $Ce^{4+}$ cannot be entirely ruled out, these observations are highly consistent with the XPS results.

After the strong reduction (SR) step, the mild oxidation (MO) process reoxidizes the $Ce^{3+}$ to $Ce^{4+}$ through the accommodation of oxygen in the nanostructure. However, unlike reduced ceria, there are no oxygen lattice vacancies in the Ce-based monolayer ($Sr_{1/2}Ce_{1/3}TiO_3$) to accommodate this extra oxygen. Thus, this work proposes that the extra oxygen is accommodated on the surface of the support, specifically on top of the last SrO layer. This final situation is somewhat similar to the one reported for layered perovskites with interstitial oxygens, such as $La_{1+x}Sr_{1-x}InO_{4+\square}$, where the additional oxygens are located between the double (001) SrO-like layers present in this type of perovskites.[51,52] In the case of the present work, the oxygens are located directly on the surface, on top of the (001) SrO plane. According to the $H_2$-TPR profiles (Fig. 2), the release of this extra oxygen during reduction in hydrogen occurs at lower temperatures (350 °C) than in pure ceria.

DFT + $U$ calculations were performed to test the proposed model and verify the improved reducibility of the system. Fig. 6 shows a supercell in which the Ce–Sr monolayer corresponds to the $Sr_{1/2}Ce_{1/3}TiO_3$ formula, featuring one-sixth cation vacancies in the monolayer of interest, and the Sr–Ti double layer on top. The extra oxygen is positioned bridging two Sr atoms on the nanostructure's surface. The calculations demonstrate that the elimination of this surface oxygen (a step necessary for the reduction of Ce) has a very low energy cost (1.4 eV). To further reduce the sample beyond this point (*i.e.*, to create $Ti^{3+}$), it becomes necessary to create an oxygen vacancy in the original perovskite structure. This process requires a significantly higher energy, amounting to 5.0 eV, which is much greater than the energy required to remove the extra surface oxygen.

As a consequence, it can be proposed that surface oxygen atoms may be responsible for the low-temperature reduction peak (at 350 °C) observed in the $CeO_2$/$SrTiO_3$-SRMO sample.

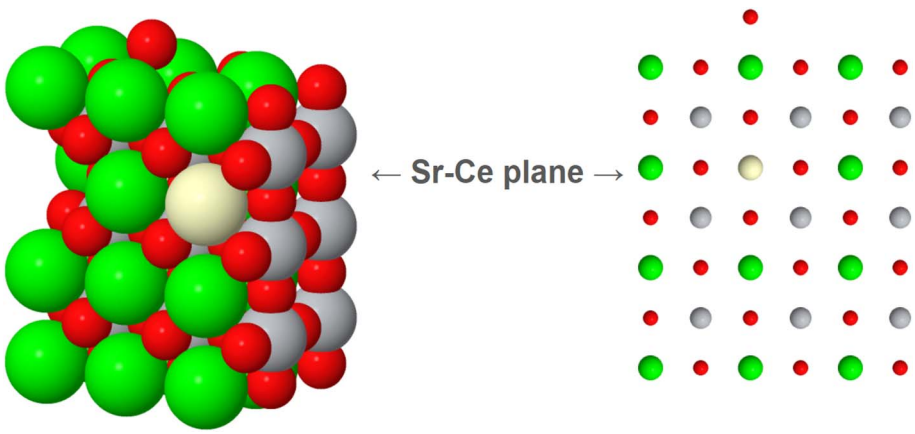


Fig. 6 Atomic model of the proposed 2D perovskite (001) nanostructure. It is necessary to introduce cation vacancies in the Sr–Ce plane to compensate for the charges of all cations. For every six cationic positions in this plane, three $Sr^{2+}$, two $Ce^{3+}$ and one cationic vacancy are considered, which is in good agreement with the proposed formula $Sr_{1/2}Ce_{1/3}TiO_3$. An additional oxygen atom has been placed on the surface, bridging two Sr atoms, to compensate for the charge excess produced by the oxidation of the two $Ce^{3+}$ cations.

Open Access Article. Published on 09 February 2026. Downloaded on 5/6/2026 9:41:51 PM.
This article is licensed under a Creative Commons Attribution 3.0 Unported Licence.

However, to make a rigorous interpretation of the TPR data, it would be necessary to study the interaction of the $H_2$ molecule in detail on the proposed models. The DFT + $U$ data provided here represents only an initial exploration of the system's reducibility.

The present data lead us to conclude that the SRMO treatment generates a 2D nanostructure similar to the pyrochlore structure reported in the $CeO_2$/YSZ system, but without any Ce/Sr cation ordering. In this particular case, a 2D ceria-perovskite based nanostructure has formed, which is susceptible to being reduced at a lower temperature compared to supported ceria nanoparticles. The amount of interstitial surface oxygens, which are the ones removed during low-temperature reduction, is directly related to the incorporation of Ce into the nanostructure. The area of the low-temperature peak accounts for most of the lanthanide loading, thereby achieving almost 100% Ce utilization.

### 3.4 Nanostructural evolution of the $CeO_2/SrTiO_3$ sample at increasing temperatures using IL-STEM and *in situ*/*ex situ* TEM/STEM experiments

Fig. S13 shows Identical Location STEM data, recorded immediately before and after the SRMO treatment. The HAADF-STEM images display the $SrTiO_3$-supported $CeO_2$ nanoparticles in the fresh sample, along with the lanthanide phase spread across the entire $SrTiO_3$ surface immediately following the treatment. Fig. 7a and b shows the same analysis over a magnified area, which very clearly illustrates the surface redistribution of Ce. The intensity profile taken across this cube before and after thermal treatment (Fig. 7c) rules out any ceria diffusion towards the cube's interior (bulk diffusion). Instead, it indicates that the thickness of the cube is slightly greater after the treatment.

This observation suggests that only a single unit cell of the perovskite has grown over the initial $SrTiO_3$ surface. The rough measured increment is less than 0.5 nm, which is very close to that expected from the formation of the 2D nanostructure. As explained, this growth could be due to the migration of some titanium and strontium cations present in the {110} bevels towards the {001} surfaces, effectively covering the previously arranged Ce-rich monolayer. A similar migration mechanism (surface self-diffusion) is expected during the sintering process observed for the bare $SrTiO_3$-SRMO sample, with the main difference being that in the case of the $CeO_2$-containing sample, the sintering stops prematurely. These experiments suggest once again that the presence of ceria promotes the stabilization of the {001} surfaces, which explains why the morphology and size of the cubes are preserved. In other words, the surface migration during the reduction treatment is mostly inhibited after the formation of the $Sr_{1/2}Ce_{1/3}TiO_3$ nanostructure.

The evolution of a couple of $SrTiO_3$-supported $CeO_2$ nanoparticles was tracked *via in situ* electron microscopy during the reduction step (Fig. S14). The HRTEM images were acquired between 500 °C and 900 °C, showing that the atomic arrangement is not modified until a very high temperature, with the atomic reconfiguration beginning from 850 °C onwards. The nanoparticle morphology rapidly disappears in the 850–900 °C temperature range, which is where the formation of the Ce-based monolayer is inferred.

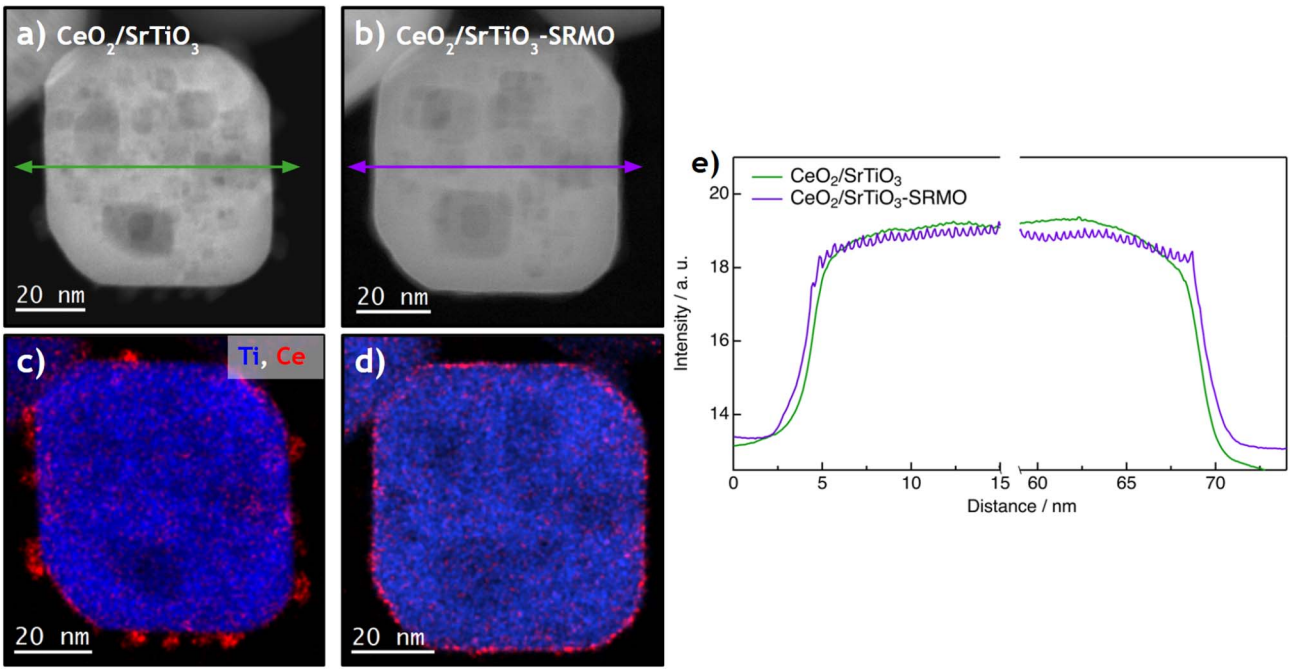


Fig. 7 High magnification IL-STEM characterization. (a) and (b) HAADF images of the same particle before and after the SRMO treatment, corresponding to the $CeO_2/SrTiO_3$ and $CeO_2/SrTiO_3$-SRMO samples, respectively. (c) and (d) XEDS elemental maps of the same area before and after the SRMO treatment, respectively. (e) Intensity profile drawn along the cube, following the green and purple arrows indicated on the HAADF images.

Open Access Article. Published on 09 February 2026. Downloaded on 5/6/2026 9:41:51 PM.
This article is licensed under a Creative Commons Attribution 3.0 Unported Licence.

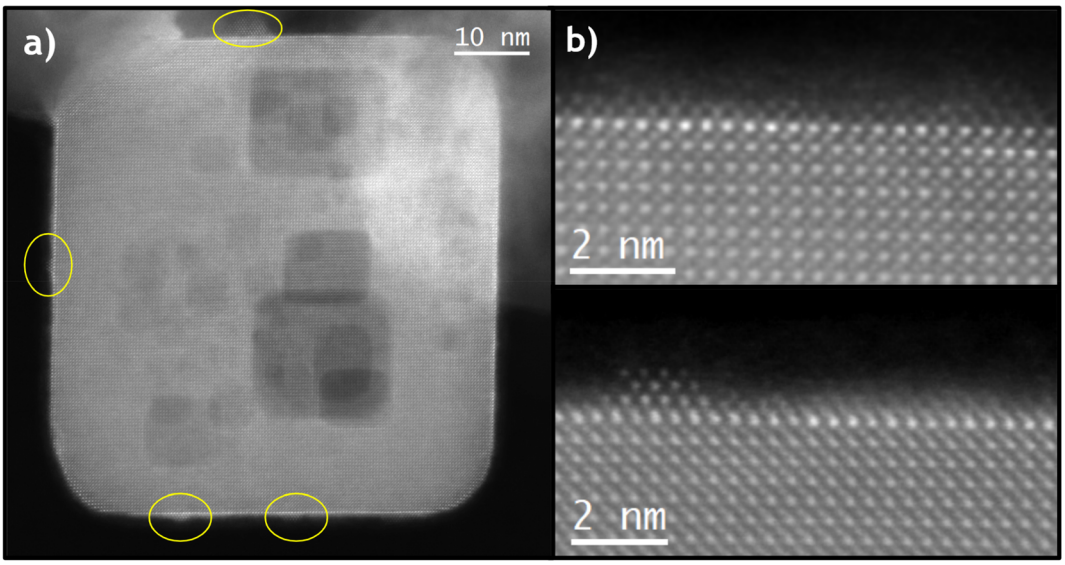


Fig. 8 STEM characterization of the $CeO_2/SrTiO_3$-SRMO sample, in which the SR step has been carried out at 700 °C. (a) $SrTiO_3$ nanocube where some regions show already the existence of the Ce-rich layer. The yellow circles mark areas where $CeO_2$ is still arranged as nanoparticles or cluster. (b) Atomic resolution HAADF images clearly illustrating that the SrO and $TiO_2$ overlayers above the Ce-rich plane are still incomplete.

To gain further insight into the structural transformations occurring at the surface level during the SRMO treatment and to correlate the temperature at which this phenomenon takes place in a conventional reactor, the $CeO_2/SrTiO_3$ sample was subjected to this thermal treatment at different temperatures (700 °C and 800 °C) during the reduction step.

Firstly, when the reduction step is carried out at 700 °C (Fig. 8), the brighter intensity at the surface of the cubes presented in the HAADF image set suggests that the formation of the $Sr_{1/2}Ce_{1/3}TiO_3$ monolayer has already begun at this temperature. However, the intensity distribution of this layer is not uniform, and there is a large fraction of remnant $CeO_2$ nanoparticles (yellow circles in Fig. 8a). HR-HAADF STEM images (Fig. 8b) reveal the presence of a diffuse layer above the surface, which may be related to cationic migration, in good agreement with the incomplete $TiO_2$ and SrO layers on top of

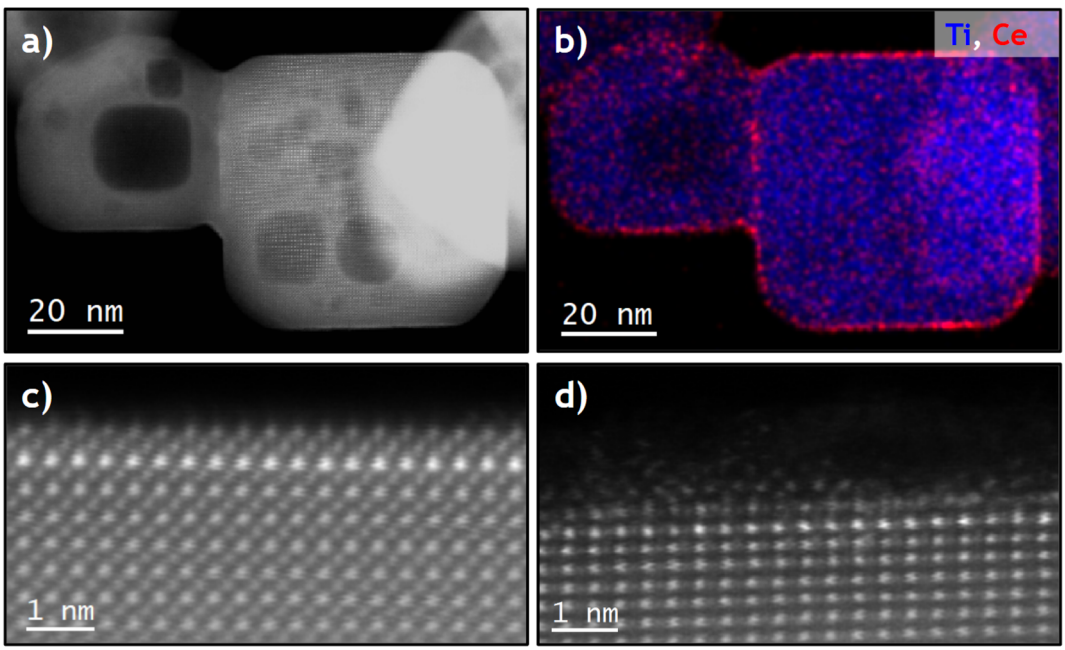


Fig. 9 STEM characterization of the $CeO_2/SrTiO_3$-SRMO sample, in which the SR step has been carried out at 800 °C. (a) and (b) HAADF image and its corresponding XEDS map, confirming that the Ce-rich layer is spread uniformly across the entire $SrTiO_3$ surface. (c) HAADF image where, unlike the surface shown in Fig. 8, the SrO and TiO2 overlayers are practically completed. (d) HAADF image revealing a situation where the perovskite layer above the Ce-rich plane is not entirely crystalline.

Open Access Article. Published on 09 February 2026. Downloaded on 5/6/2026 9:41:51 PM.
This article is licensed under a Creative Commons Attribution 3.0 Unported Licence.

the Ce-rich nanostructure. Furthermore, there are few areas in which the $TiO_2$ layer is mainly exposed at the surface, with a diffuse layer on its top but still without the crystalline SrO layer. This indicates that, although the diffusion of Sr is greater than that of Ti as reported elsewhere,[45] the migration of Ti occurs first during the formation of the 2D nanostructure.

When the severe reduction is carried out at 800 °C, Fig. 9a–c show how the dispersion of Ce and its arrangement into the single Ce/Sr monolayer are largely completed, with the subsequent $TiO_2$ and SrO layers forming the outermost perovskite unit cell. Even so, the double overlayer is not always completely crystalline (Fig. 9d), and there is still a very small remaining fraction of $CeO_2$ nanoparticles. This indicates that the formation of the 2D perovskite nanostructure is not yet fully complete, in line with the aforementioned *in situ* experiments. It is necessary to reach a temperature of 900 °C in one-hour treatments under the conditions described in the experimental section.

Finally, to evaluate the possibility of growing multiple $Sr_{1/2}$-$Ce_{1/3}TiO_3$ overlayers, a sample with a lanthanide loading equivalent to two ceria monolayers was prepared and submitted to the SRMO treatment (b-$CeO_2$/$SrTiO_3$SRMO sample). Fig. 10 reveals a more complicated situation: despite the higher ceria loading, only a single Ce-rich monolayer was formed, and the

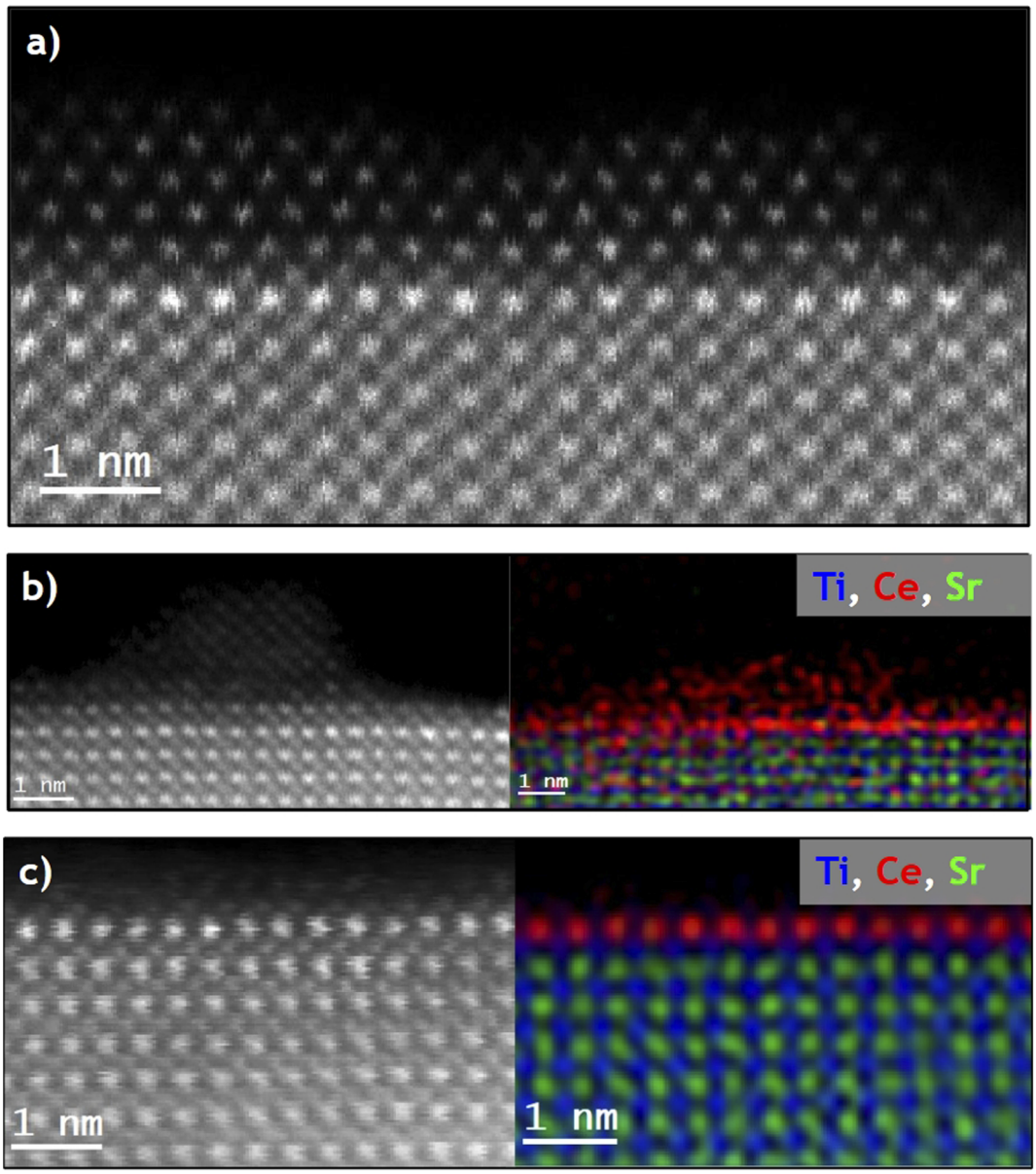


Fig. 10 STEM characterization of the b-$CeO_2$/$SrTiO_3$-SRMO sample (two ceria monolayers loading). (a) HAADF image of a representative area, showing the presence of both the Ce-rich layer and the $CeO_2$ nanoparticles. (b) HAADF and the corresponding XEDS elemental map of a region where a $CeO_2$ agglomeration coexists on top of the Ce-rich layer. (c) HAADF image and XEDS elemental map of an area where the Ce-rich layer has been clearly arranged. Note that electron beam-induced erosion during prolonged XEDS mapping likely removed the partial Sr/Ti bilayer, leaving the Ce-rich phase exposed as the outermost surface in the final image.

Open Access Article. Published on 09 February 2026. Downloaded on 5/6/2026 9:41:51 PM.
This article is licensed under a Creative Commons Attribution 3.0 Unported Licence.

excess ceria remained as $CeO_2$ nanoparticles, as confirmed by FFT analysis. This experiment suggests that the system accommodates just one cerium monolayer with an $Sr_{1/2}Ce_{1/3}$-$TiO_3$ stoichiometry, regardless of the amount of $CeO_2$ added.

To understand the formation of just one monolayer of the lanthanide phase, several DFT calculations were performed using specific models (Fig. S15), in which Ce is assumed to be in the +3 oxidation state. The first model (Fig. S15a) contains a cubic-$Ce_2O_3$ monolayer supported on top of the already-formed Ce/Sr layer. In the second model (Fig. S15b), the double Ti–Sr layer is considered on top, following the model previously described for the $CeO_2/SrTiO_3$-SRMO sample. The energy of formation of both structures is calculated using the following equations:

$$E = 1/S\,(U_{Ce_2O_3/SrCeTiO_3} - U_{SrCeTiO3} - n\cdot E_{Ce_2O_3}) \quad (2)$$

$$E = 1/S\,(U_{SrTiO_3/SrCeTiO_3} - U_{SrCeTiO_3} - n\cdot E_{SrTiO_3}) \quad (3)$$

$U_{Ce_2O_3/SrCeTiO_3}$ and $U_{SrTiO_3/SrCeTiO_3}$ correspond to the total energies of the first and second models, respectively. $U_{SrCeTiO_3}$ corresponds to the energy of the model containing just the Ce/Sr monolayer, with nothing else on top (Fig. S15c). $E_{Ce_2O_3}$ and $E_{SrTiO_3}$ correspond to the energy of a unit of bulk cubic-$Ce_2O_3$ and $SrTiO_3$, respectively. $S$ is the exposed surface area of the models. All energies were calculated after structural relaxation.

The calculated energies are 0.62 and 0.13 J $m^{-2}$ for the first and second models, respectively. This significant difference in energy indicates that, from a thermodynamic perspective, the Ce-based monolayer prefers to be covered by the Sr, Ti, and O species coming from the bulk during high-temperature reduction, rather than by an additional reduced ceria phase. Consequently, once the perovskite double layer is formed, the remaining ceria does not spread out on the surface but prefers to remain in the form of supported nanoparticles.

# 4 Conclusions

A method for the synthesis of $SrTiO_3$ nanocubes was optimized, resulting in chamfered nanocubes that primarily expose the {001} crystallographic faces with Sr termination and an occupancy close to 50%. Subsequently, quantities of $CeO_2$ equivalent to less than half (0.41) of a theoretical monolayer were deposited.

SRMO treatments were performed on both the support and the $CeO_2$-deposited sample, and TPR experiments were subsequently carried out. These experiments lead to the conclusion that the system's nanostructure is modified after the SRMO treatment: the cerium atoms occupy the vacant positions in the surface Sr layer and are partially covered by a $TiO_2$–SrO double layer. This results in the formation of a unique mixed 2D perovskite nanostructure with a Ce-layer composition close to $Sr_{1/2}Ce_{1/3}TiO_3$.

This nanostructure is covered by surface oxygen atoms resulting from the oxidation of Ce. The elimination of these surface oxygens allows for complete reduction (100% Ce utilization) at a lower temperature (350 °C), which is below the reduction temperature of highly dispersed ceria. This increase in low-temperature reducibility can be utilized in numerous catalytic applications where the formation of oxygen vacancies plays a critical role in the reaction mechanism.

The chemical behavior of the $CeO_2/SrTiO_3$ system after SRMO treatment resembles that of the $CeO_2$/YSZ system after the same process. However, in the present study, a surface perovskite forms instead of a surface pyrochlore. There is no evidence of Ce/Sr cation ordering, and the excess oxygen is not located in oxygen vacancies but rather on the surface of the 2D nanostructure, occupying a position equivalent to the interstitial oxygen found in layered mixed perovskites. This work allows us to better understand the use of surface 2D ceria nanostructures in applications involving low-temperature oxygen exchange.

# Author contributions

The manuscript was written through contributions of all authors. Experiments were carried out by RM, JMMM, CMM, ABH, LECh and JAPO. ILTEM and *In situ* S/TEM experiments were performed by RM and ABH. DFT calculations were accomplished by JAPO. Funding was achieved by JJC. Finally, JAPO wrote the original draft of the manuscript, and RM, JMMM, JJC and JAPO reviewed and edited it. All authors contributed to the discussion of results and the preparation of the manuscript.

# Conflicts of interest

There are no conflicts to declare.

# Data availability

The authors confirm that the data supporting the findings of this study are available within the article and its supplementary information (SI). Supplementary information is available. See DOI: https://doi.org/10.1039/d5ta08625f.

# Acknowledgements

The authors acknowledge support from Project PID2022-142312NB-I00 funded by MCIN/AEI/10.13039/501100011033 and "ERDF a way of making Europe"; and Project PID2023-150437OB-I00 funded by MICIU/AEI/10.13039/501100011033 and FEDER, UE. The authors also acknowledge support from Project FEDER-UCA-2024-A1-31 funded by Consejería de Universidad, Investigación e Innovación (Junta de Andalucía, Spain). Electron microscopy studies were performed at the DME-UCA node of the Spanish Unique Infrastructure (ICTS) on Electron Microscopy of Materials (ELECMI). DFT calculations were performed at the cluster CAI in the University of Cádiz.

# References

1 T. Montini, M. Melchionna, M. Monai and P. Fornasiero, Fundamentals and Catalytic Applications of CeO2-Based

Open Access Article. Published on 09 February 2026. Downloaded on 5/6/2026 9:41:51 PM.
This article is licensed under a Creative Commons Attribution 3.0 Unported Licence.

Materials, *Chem. Rev.*, 2016, **116**(10), 5987–6041, DOI: 10.1021/acs.chemrev.5b00603.

2 E. Aneggi, C. de Leitenburg, M. Boaro, P. Fornasiero, A. Trovarelli, 3 - Catalytic Applications of Cerium Dioxide. In Cerium Oxide ($CeO_2$): Synthesis, Properties and Applications, Scirè, S., Palmisano, L., *Metal Oxides*, Elsevier, 2020, pp 45–108, DOI: 10.1016/B978-0-12-815661-2.00003-7.

3 Y. Zhang, S. Zhao, J. Feng, S. Song, W. Shi, D. Wang and H. Zhang, Unraveling the Physical Chemistry and Materials Science of CeO2-Based Nanostructures, *Chem*, 2021, **7**(8), 2022–2059, DOI: 10.1016/j.chempr.2021.02.015.

4 S. Bernal, G. Blanco, J. J. Calvino, J. C. Hernández, J. A. Pérez-Omil, J. M. Pintado and M. P. Yeste, Some Recent Results on the Correlation of Nano-Structural and Redox Properties in Ceria-Zirconia Mixed Oxides, *J. Alloys Compd.*, 2008, **451**(1), 521–525, DOI: 10.1016/j.jallcom.2007.04.201.

5 S. Urban, P. Dolcet, M. Möller, L. Chen, P. J. Klar, I. Djerdj, S. Gross, B. M. Smarsly and H. Over, Synthesis and Full Characterization of the Phase-Pure Pyrochlore Ce2Zr2O7 and the κ-Ce2Zr2O8 Phases, *Appl. Catal. B Environ.*, 2016, **197**, 23–34, DOI: 10.1016/j.apcatb.2016.03.049.

6 J. Deng, C. Liang, S. Li, X. Yin, J. Wang, Y. Chen and Y. Chen, The Influence of κ-Ce2Zr2O8 Content on Three-Way Catalytic Performance, *J. Environ. Chem. Eng.*, 2023, **11**(3), 109894, DOI: 10.1016/j.jece.2023.109894.

7 J. M. Montes-Monroy, R. Manzorro, L. E. Chinchilla, W. E. Celín, J. J. Calvino and J. A. Pérez-Omil, Supported Ce/Zr Pyrochlore Monolayers as a Route to Single Cerium Atom Catalysts with Low Temperature Reducibility, *iScience*, 2023, **26**(9), 107506, DOI: 10.1016/j.isci.2023.107506.

8 M. P. Yeste, J. C. Hernández-Garrido, D. C. Arias, G. Blanco, J. M. Rodríguez-Izquierdo, J. M. Pintado, S. Bernal, J. A. Pérez-Omil and J. J. Calvino, Rational Design of Nanostructured, Noble Metal Free, Ceria–Zirconia Catalysts with Outstanding Low Temperature Oxygen Storage Capacity, *J. Mater. Chem. A*, 2013, **1**(15), 4836–4844, DOI: 10.1039/C3TA00016H.

9 J. Hutton and R. J. Nelmes, High-Resolution Studies of Cubic Perovskites by Elastic Neutron Diffraction. II. $SrTiO_3$, $KMnF_3$, $RbCaF_3$ and $CsPbCl_3$, *J. Phys. C Solid State Phys.*, 1981, **14**(12), 1713–1736, DOI: 10.1088/0022-3719/14/12/006.

10 X. Zhang, L. Zhang, B. Deng, J. Jin, C. Xu and Y. Zhang, Visible Light-Responding Perovskite Oxide Catalysts for Photo-Thermochemical CO2 Reduction, *Catal. Commun.*, 2020, **138**, 105955, DOI: 10.1016/j.catcom.2020.105955.

11 J. Ling, K. Wang, Z. Wang, H. Huang and G. Zhang, Enhanced Piezoelectric-Induced Catalysis of SrTiO3 Nanocrystal with Well-Defined Facets under Ultrasonic Vibration, *Ultrason. Sonochem.*, 2020, **61**, 104819, DOI: 10.1016/j.ultsonch.2019.104819.

12 C. Avcıoğlu, S. Avcıoğlu, M. F. Bekheet and A. Gurlo, Photocatalytic Overall Water Splitting by SrTiO3: Progress Report and Design Strategies, *ACS Appl. Energy Mater.*, 2023, **6**(3), 1134–1154, DOI: 10.1021/acsaem.2c03280.

13 M. RaeisianAsl, S. Jouybar, S. Sarabadani Tafreshi and L. Naji, Exploring the Key Features for Enhanced SrTiO3 Functionality: A Comprehensive Overview, *Mater. Today Sustain.*, 2025, **29**, 101072, DOI: 10.1016/j.mtsust.2025.101072.

14 Z. Chen, W. Liu, L. Zheng, Q. Chen, Y. Liu, S. Lan and M. Zhu, Enhancing Production of Hydrogen and Simultaneous Degradation of Ciprofloxacin over Sn Doped SrTiO3 Piezocatalyst, *Sep. Purif. Technol.*, 2025, **353**, 128307, DOI: 10.1016/j.seppur.2024.128307.

15 M. Humayun, L. Xu, L. Zhou, Z. Zheng, Q. Fu and W. Luo, Exceptional Co-Catalyst Free Photocatalytic Activities of B and Fe Co-Doped SrTiO3 for CO2 Conversion and H2 Evolution, *Nano Res.*, 2018, **11**(12), 6391–6404, DOI: 10.1007/s12274-018-2164-z.

16 K. Aravinthkumar, E. Praveen, A. Jacquline Regina Mary and C. Raja Mohan, Investigation on SrTiO3 Nanoparticles as a Photocatalyst for Enhanced Photocatalytic Activity and Photovoltaic Applications, *Inorg. Chem. Commun.*, 2022, **140**, 109451, DOI: 10.1016/j.inoche.2022.109451.

17 Z. Zhu, J. Zhou, Q. Li, Z. Liu, Q. Deng, Z. Zhou, C. Li, L. Fu, J. Zhou, H. Li, Q. Zhang and K. Wu, Preparation of Heterostructured Cu-CeO2/SrTiO3 Catalysts by Rapid Plasma Exsolution for Photothermal Reverse Water Gas Shift Reaction, *J. $CO_2$ Util.*, 2024, **80**, 102665, DOI: 10.1016/j.jcou.2023.102665.

18 B. Kayaalp, K. Klauke, M. Biesuz, A. Iannaci, V. M. Sglavo, M. D'Arienzo, H. Noei, S. Lee, W. Jung and S. Mascotto, Surface Reconstruction under the Exposure of Electric Fields Enhances the Reactivity of Donor-Doped $SrTiO_3$, *J. Phys. Chem. C*, 2019, **123**(27), 16883–16892, DOI: 10.1021/acs.jpcc.9b04620.

19 J. Ling, K. Wang, Z. Wang, H. Huang and G. Zhang, Enhanced Piezoelectric-Induced Catalysis of SrTiO3 Nanocrystal with Well-Defined Facets under Ultrasonic Vibration, *Ultrason. Sonochem.*, 2020, **61**, 104819, DOI: 10.1016/j.ultsonch.2019.104819.

20 M. Dogan and S. Ismail-Beigi, Ferroelectric $ZrO_2$ Monolayers as Buffer Layers between $SrTiO_3$ and Si, *J. Phys. Chem. C*, 2019, **123**(24), 15053–15061, DOI: 10.1021/acs.jpcc.9b03069.

21 U. K. N. Din, T. H. T. Aziz, M. M. Salleh and A. A. Umar, Synthesis of Crystalline Perovskite-Structured SrTiO3 Nanoparticles Using an Alkali Hydrothermal Process, *Int. J. Miner. Metall. Mater.*, 2016, **23**(1), 109–115, DOI: 10.1007/s12613-016-1217-0.

22 G. S. Foo, Z. D. Hood and Z. Wu, Shape Effect Undermined by Surface Reconstruction: Ethanol Dehydrogenation over Shape-Controlled $SrTiO_3$ Nanocrystals, *ACS Catal.*, 2018, **8**(1), 555–565, DOI: 10.1021/acscatal.7b03341.

23 V. Kalyani, B. S. Vasile, A. Ianculescu, A. Testino, A. Carino, M. T. Buscaglia, V. Buscaglia and P. Nanni, Hydrothermal Synthesis of $SrTiO_3$ : Role of Interfaces, *Cryst. Growth Des.*, 2015, **15**(12), 5712–5725, DOI: 10.1021/acs.cgd.5b00770.

24 H. Shen, Y. Lu, Y. Wang, Z. Pan, G. Cao, X. Yan and G. Fang, Low Temperature Hydrothermal Synthesis of SrTiO3 Nanoparticles without Alkali and Their Effective

Open Access Article. Published on 09 February 2026. Downloaded on 5/6/2026 9:41:51 PM.
This article is licensed under a Creative Commons Attribution 3.0 Unported Licence.

Photocatalytic Activity, *J. Adv. Ceram.*, 2016, **5**(4), 298–307, DOI: 10.1007/s40145-016-0203-3.

25 V. Solokha, D. Garai, A. Wilson, D. A. Duncan, P. K. Thakur, K. Hingerl and J. Zegenhagen, Water Splitting on Ti-Oxide-Terminated SrTiO3(001), *J. Phys. Chem. C*, 2019, **123**(28), 17232–17238, DOI: 10.1021/acs.jpcc.9b01730.

26 H. Wang, H. Zhang, H. Zhang, J. Bai, J. Ren and S. Wang, 001) CeO2 Films Epitaxially Grown on SrTiO3 (001) Substrates by Pulsed Laser Deposition Using a Metallic Ce Target, *Vacuum*, 2013, **87**, 81–83, DOI: 10.1016/j.vacuum.2012.07.012.

27 P. P. Dholabhai, J. A. Aguiar, A. Misra and B. P. Uberuaga, Defect Interactions with Stepped $CeO_2/SrTiO_3$ Interfaces: Implications for Radiation Damage Evolution and Fast Ion Conduction, *J. Chem. Phys.*, 2014, **140**(19), 194701, DOI: 10.1063/1.4876225.

28 B. Zhu, G. Schusteritsch, W. Li, W. Xing, R. Yu, C. J. Pickard and J. L. MacManus-Driscoll, Structure and Ionic Conduction Enhancement Mechanisms at CeO2/SrTiO3 Heterointerfaces, *Appl. Phys. Rev.*, 2024, **11**(2), 021420, DOI: 10.1063/5.0185746.

29 Z. Zhu, J. Zhou, Q. Li, Z. Liu, Q. Deng, Z. Zhou, C. Li, L. Fu, J. Zhou, H. Li, Q. Zhang and K. Wu, Preparation of Heterostructured Cu-CeO2/SrTiO3 Catalysts by Rapid Plasma Exsolution for Photothermal Reverse Water Gas Shift Reaction, *J. $CO_2$ Util.*, 2024, **80**, 102665, DOI: 10.1016/j.jcou.2023.102665.

30 Z. Zhang, X. Han, J. Zhang, Y. Dong, J. Zhao, Q. Xu and N. Zhang, Revolutionizing Photothermal $CO_2$ Hydrogenation with Ceria-Based Catalysts, *Nano Res.*, 2025, **18**(1), 94906998, DOI: 10.26599/NR.2025.94906998.

31 C. Arias-Duque, E. Bladt, M. A. Muñoz, J. C. Hernández-Garrido, M. A. Cauqui, J. M. Rodríguez-Izquierdo, G. Blanco, S. Bals, J. J. Calvino, J. A. Pérez-Omil and M. P. Yeste, Improving the Redox Response Stability of Ceria-Zirconia Nanocatalysts under Harsh Temperature Conditions, *Chem. Mater.*, 2017, **29**(21), 9340–9350, DOI: 10.1021/acs.chemmater.7b03336.

32 S. Shetty, S. K. Sinha, R. Ahmad, A. K. Singh, G. Van Tendeloo and N. Ravishankar, Existence of Ti2+ States on the Surface of Heavily Reduced SrTiO3 Nanocubes, *Chem. Mater.*, 2017, **29**(23), 9887–9891, DOI: 10.1021/acs.chemmater.7b04113.

33 M. P. Yeste, J. C. Hernández, S. Bernal, G. Blanco, J. J. Calvino, J. A. Pérez-Omil and J. M. Pintado, Redox Behavior of Thermally Aged Ceria−Zirconia Mixed Oxides. Role of Their Surface and Bulk Structural Properties, *Chem. Mater.*, 2006, **18**(11), 2750–2757, DOI: 10.1021/cm060635i.

34 W. Kraus and G. Nolze, POWDER CELL – a Program for the Representation and Manipulation of Crystal Structures and Calculation of the Resulting X-Ray Powder Patterns, *J. Appl. Crystallogr.*, 1996, **29**(3), 301–303, DOI: 10.1107/S0021889895014920.

35 N. Fairley, V. Fernandez, M. Richard-Plouet, C. Guillot-Deudon, J. Walton, E. Smith, D. Flahaut, M. Greiner, M. Biesinger, S. Tougaard, D. Morgan and J. Baltrusaitis, Systematic and Collaborative Approach to Problem Solving Using X-Ray Photoelectron Spectroscopy, *Appl. Surf. Sci. Adv.*, 2021, **5**, 100112, DOI: 10.1016/j.apsadv.2021.100112.

36 S. Bernal, F. J. Botana, J. Calvino, C. López, A. Pérez-Omil and M. Rodríguez-Izquierdo, J. High-Resolution Electron Microscopy Investigation of Metal–Support Interactions in Rh/TiO 2, *J. Chem. Soc. Faraday Trans.*, 1996, **92**(15), 2799–2809, DOI: 10.1039/FT9969202799.

37 S. Bernal, F. J. Botana, J. J. Calvino, C. López-Cartes, J. A. Pérez-Omil and J. M. Rodríguez-Izquierdo, The Interpretation of HREM Images of Supported Metal Catalysts Using Image Simulation: Profile View Images, *Ultramicroscopy*, 1998, **72**(3), 135–164, DOI: 10.1016/S0304-3991(98)00009-6.

38 J. A. Pérez-Omil, TEMserver, http://temserver.uca.es, accessed 2022-10-17.

39 E. J. Kirkland, Computation in Electron Microscopy, *Acta Crystallogr. Sect. Found. Adv.*, 2016, **72**(1), 1–27, DOI: 10.1107/S205327331501757X.

40 P. Giannozzi, S. Baroni, N. Bonini, M. Calandra, R. Car, C. Cavazzoni, D. Ceresoli, G. L. Chiarotti, M. Cococcioni, I. Dabo, A. D. Corso, S. de Gironcoli, S. Fabris, G. Fratesi, R. Gebauer, U. Gerstmann, C. Gougoussis, A. Kokalj, M. Lazzeri, L. Martin-Samos, N. Marzari, F. Mauri, R. Mazzarello, S. Paolini, A. Pasquarello, L. Paulatto, C. Sbraccia, S. Scandolo, G. Sclauzero, A. P. Seitsonen, A. Smogunov, P. Umari and R. M. Wentzcovitch, QUANTUM ESPRESSO: A Modular and Open-Source Software Project for Quantum Simulations of Materials, *J. Phys. Condens. Matter*, 2009, **21**(39), 395502, DOI: 10.1088/0953-8984/21/39/395502.

41 A. Dal Corso, Pseudopotentials Periodic Table: From H to Pu, *Comput. Mater. Sci.*, 2014, **95**, 337–350, DOI: 10.1016/j.commatsci.2014.07.043.

42 M. Topsakal and R. M. Wentzcovitch, Accurate Projected Augmented Wave (PAW) Datasets for Rare-Earth Elements (RE=La–Lu), *Comput. Mater. Sci.*, 2014, **95**, 263–270, DOI: 10.1016/j.commatsci.2014.07.030.

43 I. Timrov, N. Marzari and M. H. P. – A. Cococcioni, Code for the Calculation of Hubbard Parameters Using Density-Functional Perturbation Theory, *Comput. Phys. Commun.*, 2022, **279**, 108455, DOI: 10.1016/j.cpc.2022.108455.

44 R. Manzorro, W. E. Celín, J. A. Pérez-Omil, J. J. Calvino and S. Trasobares, Improving the Activity and Stability of YSZ-Supported Gold Powder Catalyst by Means of Ultrathin, Coherent, Ceria Overlayers. Atomic Scale Structural Insights, *ACS Catal.*, 2019, **9**(6), 5157–5170, DOI: 10.1021/acscatal.8b04412.

45 H. Du, C.-L. Jia and J. Mayer, Surface Atomic Structure and Growth Mechanism of Monodisperse {1 0 0}-Faceted Strontium Titanate Zirconate Nanocubes, *Chem. Mater.*, 2016, **28**(2), 650–656, DOI: 10.1021/acs.chemmater.5b04486.

46 Z.-K. Han, L. Zhang, M. Liu, M. V. Ganduglia-Pirovano and Y. Gao, The Structure of Oxygen Vacancies in the Near-Surface of Reduced CeO2 (111) Under Strain, *Front. Chem.*, 2019, **7**, 436, DOI: 10.3389/fchem.2019.00436.

47 M. Dogan and S. Ismail-Beigi, Ferroelectric ZrO2 Monolayers as Buffer Layers between SrTiO3 and Si, *J. Phys. Chem. C*, 2019, **123**(24), 15053–15061, DOI: 10.1021/acs.jpcc.9b03069.

Open Access Article. Published on 09 February 2026. Downloaded on 5/6/2026 9:41:51 PM.
This article is licensed under a Creative Commons Attribution 3.0 Unported Licence.

48 G. Sánchez-Santolino, J. Tornos, F. Y. Bruno, F. A. Cuellar, C. Leon, J. Santamaría, S. J. Pennycook and M. Varela, Characterization of Surface Metallic States in SrTiO3 by Means of Aberration Corrected Electron Microscopy, *Ultramicroscopy*, 2013, **127**, 109–113, DOI: 10.1016/j.ultramic.2012.07.013.

49 B. Ullah, W. Lei, X.-Q. Song, X.-H. Wang and W.-Z. Lu, Perovskite Structure and Low Frequency Relaxor- like-Dielectric Response of (Sr,Ce)TiO3 Solid Solution, *Ceram. Int.*, 2017, **43**(18), 16376–16383, DOI: 10.1016/j.ceramint.2017.09.012.

50 X. Chen, C. Li, B. Li, Y. Ying, S. Ye, D. N. Zakharov, S. Hwang, J. Fang, G. Wang, Y.-J. Hu and G. Zhou, Surface Self-Diffusion Induced Sintering of Nanoparticles, *ACS Nano*, 2024, **18**(45), 31160–31173, DOI: 10.1021/acsnano.4c09056.

51 A. Chroneos, R. V. Vovk, I. L. Goulatis and L. I. Goulatis, Oxygen Transport in Perovskite and Related Oxides: A Brief Review, *J. Alloys Compd.*, 2010, **494**(1), 190–195, DOI: 10.1016/j.jallcom.2010.01.071.

52 L. Troncoso, J. A. Alonso and A. Aguadero, Low Activation Energies for Interstitial Oxygen Conduction in the Layered Perovskites La1+xSr1−xInO4+δ, *J. Mater. Chem. A*, 2015, **3**(34), 17797–17803, DOI: 10.1039/C5TA03185K.